

PointRecon: Online Point-based 3D Reconstruction via Ray-based 2D-3D Matching

Chen Ziwen¹ Zexiang Xu² Li Fuxin¹

¹Oregon State University ²Adobe Research

Abstract

We propose a novel online, point-based 3D reconstruction method from posed monocular RGB videos. Our model maintains a global point cloud representation of the scene, continuously updating the features and 3D locations of points as new images are observed. It expands the point cloud with newly detected points while carefully removing redundancies. The point cloud updates and the depth predictions for new points are achieved through a novel ray-based 2D-3D feature matching technique, which is robust against errors in previous point position predictions. In contrast to offline methods, our approach processes infinite-length sequences and provides real-time updates. Additionally, the point cloud imposes no pre-defined resolution or scene size constraints, and its unified global representation ensures view consistency across perspectives. Experiments on the ScanNet dataset show that our method achieves comparable quality among online MVS approaches. Project page: <https://arthurhero.github.io/projects/pointrecon/>

1. Introduction

3D reconstruction is a fundamental problem in computer vision. The ability to recover the 3D geometry of a scene from a set of posed RGB images, known as multi-view stereo (MVS), enables numerous applications, including object retrieval, robotics, and computer-aided 3D design. Unlike methods relying on expensive depth sensors such as LiDAR, RGB-based MVS offers a cost-effective alternative, eliminating calibration errors and synchronization issues associated with multiple sensors. Among other reconstruction scenarios, online MVS methods are particularly well-suited for reconstructing large scenes from extremely long image sequences.

Deep learning has enabled a wide range of MVS methods. Depth prediction-based approaches [2, 8, 12, 13, 16, 26, 33, 34] accumulate features from multiple views into a

per-view cost volume to regress depth maps, while volumetric methods [1, 10, 15, 23, 28, 30] aggregate features into a global voxel grid to predict occupancy or TSDF values. Point cloud-based methods [4, 18] directly estimate surface point positions. However, depth prediction methods regress depth maps independently for each image, which can lead to inconsistencies across views. Volumetric methods maintain a global voxel grid, but require predefined voxel sizes and suffer from high memory costs at high resolutions, resulting in coarse meshes. Additionally, they are limited to bounded areas and cannot extend to an infinite horizon, despite the advantages of using cameras.

A globally consistent 3D point cloud representation addresses some of these drawbacks. It is a sparse representation that significantly reduces memory consumption compared to volumetric methods. Furthermore, point clouds do not require predefined voxel sizes and can adaptively represent surface details with varying densities, allowing for greater detail in areas that need it. However, existing point cloud-based MVS methods typically rely on iterative optimization [4, 17], making them unsuitable for online algorithms.

In this paper, we propose PointRecon, an online point-based MVS method that maintains a global feature-augmented point cloud for scene representation. When a new image is observed, we match its 2D features with existing 3D points using our novel ray-based 2D-3D matching technique, which is robust against errors in previous position predictions. We begin with matching each 3D feature in the point cloud with the image features by projecting the 3D camera ray onto the image plane, similar to an epipolar line. The 3D feature is then compared against the 2D features along the projected ray, followed by an update of its feature and position. Next, we match each 2D feature with the existing point cloud by extending its corresponding camera ray into the 3D space. The 2D feature is similarly compared against the 3D features along this ray, informing the next depth prediction step. Note that since point clouds are compact representations, they contain features only on the predicted surface, which may sometimes be in incor-

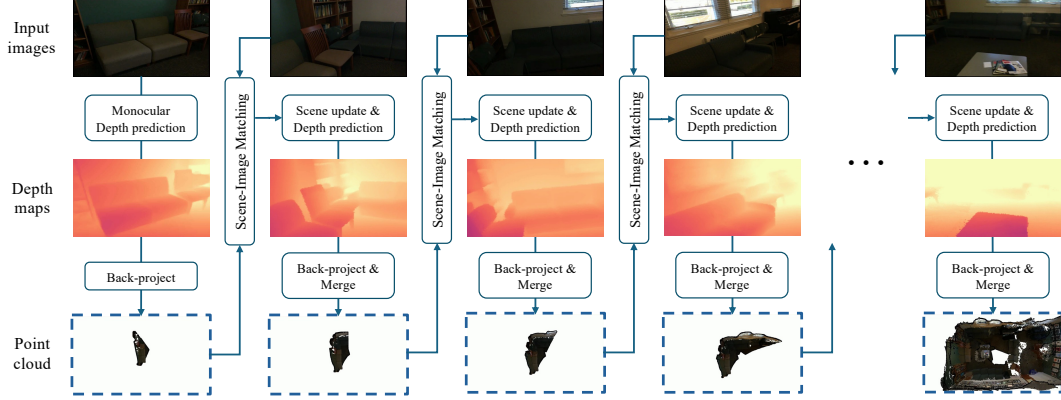


Figure 1. **Workflow of PointRecon.** We begin with monocular depth prediction for the first image, lifting 2D points into 3D space to form the initial point cloud. For each subsequent image, we perform feature matching between the 2D image features and the 3D point cloud features to update the features and positions of the point cloud and to predict depth for the 2D image. Finally, the new points are merged with the existing point cloud.

rect location. Naively searching for the nearest 3D points along the camera ray risks missing true matches. However, the camera rays of a matching pair must intersect. Thus, we enhance robustness by gathering 3D neighbors based on the minimal ray distance to the target 2D feature’s camera ray. Finally, we merge the new points from the image into the existing point cloud using a carefully designed merging module that effectively removes redundant points. We also provide simple algorithms to render depth maps and fuse 3D meshes from the point cloud.

It is important to note that the scope of online MVS methods differs from that of SLAM methods [22, 32, 37–39]. Our method recovers geometry from a sequence of posed images and operates purely in a feed-forward manner, while SLAM methods estimate both camera pose and geometry, typically involving optimization steps like the Gauss-Newton algorithm and bundle adjustment.

In summary, our contributions are:

- We propose an online point-based MVS method that maintains a feature-augmented 3D point cloud, **unconstrained by input sequence length, predefined voxel resolutions or scene sizes, while ensuring consistency among viewpoints.**
- We introduce a robust ray-based 2D-3D matching technique for aligning the 3D point cloud with 2D points from incoming images for position estimation.
- Our results on the popular ScanNetv2 dataset demonstrate that our approach achieves comparable quality to existing online methods while providing the flexibility mentioned above.

2. Related Work

We summarize previous MVS methods, categorizing them based on their surface representations: depth maps, volumetric TSDF grids, and point clouds.

Depth Prediction via Multi-view Stereo Matching.

Depth can be inferred from image patch similarity between two posed cameras viewing the same object [24, 25], but manually designed measures are often unreliable. CNN-based methods [20, 35] improve this by learning patch similarity, though they still lack global context and require post-processing. GC-Net [16] introduces cost volumes and 3D convolutions for global context, while PSM-Net [2] further improves it with multi-scale feature maps. DeepMVS [12] and MVSNet [34], both extend stereo matching to multiple views, with DeepMVS using plane-sweep volumes and MVSNet introducing a camera frustum-based 3D cost volume. MVDepthNet [33] further refines this process by compressing features into a single volume for efficient 2D convolution. DPSNet [13] improves results by matching deeper features, DeepVideoMVS [8] integrates reconstruction history with a recurrent network, and SimpleRecon [26] further enhances depth map quality by incorporating geometric metadata into the cost volume. While depth map-based MVS methods break down large scenes for faster inference, without a unified scene representation, the independently predicted depth maps fail to ensure consistent views.

Volumetric TSDF Regression. Instead of predicting depth maps, some methods directly generate global surfaces from cost volumes. LSM [15] back-projects features into a global voxel grid for each image and fuses them to regress global voxel occupancy. Atlas [23] extends this to scenes by accumulating features into a global voxel grid and using 3D convolution to regress TSDF values. NeuralRecon [30] introduces an online approach that incrementally constructs and fuses local grids with a global grid using a GRU, while also sparsifying fine grids based on coarse predictions. Building on this, TransformerFusion [1] leverages transformers to selectively fuse image features into the voxel grid. Further improvements are made by VisFusion [10], which incorpo-

rates ray-based sparsification, and DG-Recon [14], which enhances the process with monocular depth priors. More recent offline methods like VoRTX [28] incorporate ray direction and depth for view-aware attention, while FineRecon [29] and CVRecon [9] enhance results through fine-grained supervision and cost-volume integration. While volumetric methods offer consistency and can infer unseen surfaces, they rely on predefined grids (often 4cm in size), limiting their ability to capture finer details.

Point Cloud-based Reconstruction. Early methods like [18] extract keypoints, back-project them into 3D space to form a point cloud, and optimize a surface over it. Deep learning-based approaches like Point-MVSNet [4] predict a coarse depth map, back-project to a point cloud, augment it with multi-view features, and iteratively refine point positions or depth maps. However, these methods are not online and focus primarily on object datasets. To the best of our knowledge, our method is the first online point-based MVS approach generalized to large scenes. Recently, Gaussian splatting-based reconstruction methods have gained attention, where each Gaussian can be viewed as a point with scale and opacity. While the original 3D GS [17] requires per-scene optimization, recent methods have extended it to feed-forward reconstruction [3, 5, 31, 36]. In particular, Long-LRM [41] achieves scene-level GS reconstruction from long-sequence input in a fully feed-forward manner. However, these methods mainly focus on color rendering from novel views, whereas the primary goal of MVS is to reconstruct geometry. Without explicit depth supervision, Gaussian-based methods often suffer from the “floater” issue, where translucent Gaussian clouds appear at incorrect locations. Our method could serve as a strong initialization for future online, feed-forward, large-scene Gaussian reconstructions.

3. Method

We propose PointRecon, an online, point-based MVS method that incrementally builds and updates a global 3D point cloud from a sequence of posed monocular RGB images.

The core idea of our approach is to represent the scene using a global, feature-augmented point cloud $\mathbf{Q} = \{\mathbf{q}_1, \mathbf{q}_2, \dots\}$, which is continuously updated with new observations. Each point $\mathbf{q}_i = (p_i, f_i, r_i, z_i, \sigma_i, c_i)$ consists of 3D position $p_i \in \mathbb{R}^3$, feature vector $f_i \in \mathbb{R}^C$, initial ray direction $r_i \in \mathbb{R}^3$ (unit vector), distance to the originating camera $z_i \in \mathbb{R}^+$, Gaussian standard deviation $\sigma_i \in \mathbb{R}^+$ of the position along r_i , and confidence score $c_i \in \mathbb{R}$. Points can move along their original camera ray based on new information from incoming images $\mathbf{I}_t \in \mathbb{R}^{H \times W \times 3}$ at time t . In the following, we use p° for 2D positions and p for their corresponding 3D positions. Furthermore, we use r_i to denote the unit direction vector of a camera ray, while

\mathcal{R}_i represents the set of all points lying along that ray, to avoid any confusion in notation.

Our key contribution is a ray-based feature matching strategy between 3D points and 2D image pixels, which is robust to errors in the initial 3D positions. This matching is performed in two steps: 1) For each 3D point within the camera frustum of a new image, we project its camera ray onto the image plane to form an epipolar line and gather 2D neighbors near this line (Fig. 2). These 2D neighbors are used to update the point’s feature and refine its 3D position (Sec. 3.2). 2) For each 2D point in the image, we uniformly sample positions along its camera ray and gather 3D points with the nearest camera rays to form a neighborhood (Fig. 3). Feature matching between the 2D point and the 3D neighbors is performed for depth prediction (Sec. 3.3). The 2D points are then back-projected into 3D space based on their predicted depth. Finally, we merge the new 3D points with the existing point cloud, removing redundant points by comparing confidence scores of points that project onto the same pixel and keeping only the most confident ones (Sec. 3.4).

3.1. Backbone, Feature Pyramid and Monocular Depth Prediction

We first pass the image \mathbf{I}_t through an image encoder to produce a set of multi-level feature maps $\{\mathbf{F}^l\}_{l=1}^4$, where level 1 is the coarsest and level 4 the finest. While our approach is compatible with any image encoder, such as ResNets [11], we specifically use AutoFocusFormer [40], a transformer-based encoder that excels at preserving key details by automatically locating important points during downsampling. This results in non-uniform 2D point cloud feature maps, represented as $\mathbf{F}^l = \{(p_1^\circ, f_1), (p_2^\circ, f_2), \dots\}$ at each level.

Next, we enhance the feature maps $\{\mathbf{F}^l\}_{l=1}^4$ by constructing a feature pyramid, propagating information from coarser to finer levels. For each level $l \in \{2, 3, 4\}$, we update \mathbf{F}^l by attending to all coarser levels \mathbf{F}^k (where $k \leq l$) using a transformer block (attention + MLP), starting from the coarsest and moving to the finest.

For the first image in the stream, we perform monocular depth estimation. A linear layer predicts a positive depth value from each point’s feature vector f_i , along with a positive standard deviation σ_i and a confidence score c_i . We then back-project the 2D features into 3D using the camera intrinsics and pose, forming the initial multi-level point cloud $\{\mathbf{Q}^l\}_{l=1}^4$. The confidence score c_i , a logit in \mathbb{R} , is used later during point cloud merging (Sec. 3.4). While monocular depth estimation is prone to ambiguity, our method quickly corrects errors through scene update.

3.2. Scene Update

We begin with a multi-level point cloud $\{\mathbf{Q}^l\}_{l=1}^4$ that may contain position errors. After computing the multi-level fea-

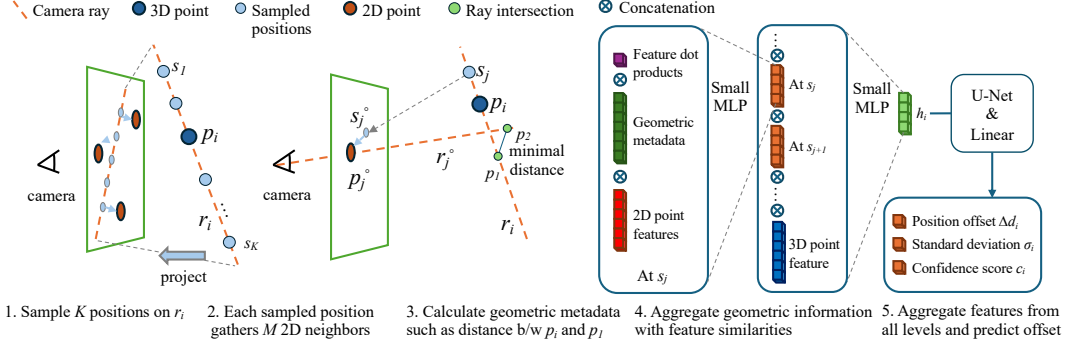


Figure 2. **Illustration of the scene update step** (single level shown for simplicity). For a point p_i in the point cloud, we uniformly sample K positions along its ray and project them onto the image plane. Each projected sampled position selects M nearest neighbors in the 2D feature map. We then compute the feature dot product between p_i and each neighbor, along with geometric metadata, such as the distance between p_i and the crossing of their camera rays. The 3D point uses both geometric information and feature similarities to determine its position adjustment along the ray.

ture maps $\{\mathbf{F}_t^l\}_{l=1}^4$ for a new image \mathbf{I}_t , we update the visible portion of the point cloud. To do this, we project the 3D camera rays onto the image plane of \mathbf{I}_t , creating epipolar lines, and match the 3D point features with the 2D features near these lines. Specifically, for each 3D scene point \mathbf{q}_i , we uniformly sample K positions along its camera ray, centered at its 3D location p_i . These positions are then projected onto the image plane of \mathbf{I}_t , with each finding M nearest 2D features from \mathbf{F} . In total, this process collects KM 2D feature points along each ray.

To reduce the memory cost of feature matching, we first reduce the channel size of both the 2D and 3D features from C to 32 using a linear layer across all levels. Then, we compute the dot product between the 3D and the neighboring 2D features. However, for the model to determine the direction in which a point should move, it's not enough to just compute feature similarities with the neighbors; the model also needs to know *where* the neighbors are, especially given the non-uniform nature of point clouds. To address this, we append geometric metadata to the feature similarity.

The general idea is that if a 3D point \mathbf{q}_i matches with a 2D image point p_j° , we should move \mathbf{q}_i to the intersection of its camera ray r_i and the camera ray r_j° of p_j° (the ray from the current camera shooting through p_j°) (see Fig. 2). To enable this adjustment, we gather metadata about the ray intersection. Specifically, we define the intersection as the pair of points—one on each ray—connected by the shortest distance between r_i and r_j° :

$$p_1(r_i, r_j^\circ) = \arg \min_{p \in \mathcal{R}_i} \min_{p' \in \mathcal{R}_j^\circ} \|p - p'\| \quad (1)$$

$$p_2(r_i, r_j^\circ) = \arg \min_{p' \in \mathcal{R}_j^\circ} \min_{p \in \mathcal{R}_i} \|p - p'\| \quad (2)$$

, where p_1 lies on the ray r_i and p_2 lies on the ray r_j° . Additionally, we include other metadata such as the ray angle and point distance to further support the reliability of this matching. Concretely, for a 3D point \mathbf{q}_i with camera ray

r_i , a sampled position s_j on r_i , and a 2D neighbor p_j° with camera ray r_j° , the list of geometric metadata includes:

- the signed distance between p_i (the 3D location of \mathbf{q}_i) and p_1 : $(p_1 - p_i) \cdot r_i$
- the signed distance between p_i and s_j : $(s_j - p_i) \cdot r_i$
- the signed distance between s_j and p_1 : $(p_1 - s_j) \cdot r_i$
- the distance between p_1 and the originating camera of p_i : $\|p_1 - (p_i - z_i \cdot r_i)\|$
- the depth of p_1 with respect to the current camera
- the distance between the two rays: $\|p_1 - p_2\|$
- the cosine angle between r_i and r_j° : $r_i \cdot r_j^\circ$
- the distance between the 2D projection of s_j and p_j° : $\|s_j^\circ - p_j^\circ\|$
- the probability density at p_1 within the Gaussian distribution centered at p_i with standard deviation σ_i : $\frac{1}{\sigma_i \sqrt{2\pi}} \exp(-\frac{1}{2}(\frac{p_1 - p_i}{\sigma_i})^2)$
- a binary mask indicating whether s_j lies inside the current camera frustum

We concatenate the dot products, metadata, and reduced 2D features at each sampled position and pass them through a small MLP. Next, we concatenate the output vectors from all sampled positions along with the reduced feature of \mathbf{q}_i , feeding them through another small MLP. The final output vector h_i represents the information that \mathbf{q}_i gains from the image \mathbf{I}_t .

Finally, we use a small U-Net to aggregate features across all levels. During the encoding process, each level first attends to the features one level finer and then to itself. In the decoding process, each level first attends to the features one level coarser and then to itself. From the updated feature h_i , we use a linear layer to predict a position offset Δd_i along the ray, as well as an updated standard deviation σ_i and a confidence score c_i . At levels other than the coarsest, we leverage point movements from the coarser point cloud to guide the offset predictions. Specifically, each point at these levels collects the predicted offsets from nearby points in the coarser point cloud, projects these

offsets onto its own ray, interpolates them using inverse distance weights, and appends the result to h_i before making the final offset prediction. Additionally, we append h_i to the original point features f_i and pass them through a linear layer to produce the final updated features for the scene.

3.3. Depth Prediction

Next, we predict the depth values for the 2D points. This feature matching process closely mirrors the one used in scene update. For each 2D point p_i° , let r_i° represent the ray passing through it from the current camera view. We begin by predicting a rough depth value for p_i° using the monocular depth prediction module. Then, we uniformly sample K positions along r_i° within a range centered around the predicted 3D position p_i' . Each sampled position identifies the M nearest rays from the scene, resulting in a collection of KM 3D neighbors along the ray r_i° .

We opt to find the nearest rays, rather than the nearest points, because the point positions are predicted and might be inaccurate. Additionally, by first sampling positions along r_i° we avoid concentrating matches at shallow depths. This occurs because ray intersections from neighboring cameras tend to cluster more densely at shallow depths, which would skew the matching process if we directly searched for rays closest to r_i° .

We again compute the feature dot product between the reduced 2D and 3D features. As in the scene update step, we append geometric metadata to the dot products. The core idea is that if the 2D point p_i° matches with a 3D ray r_j , then the depth of the crossing between r_i° and r_j is likely the correct depth for p_i° . Concretely, for a 2D point p_i° with camera ray r_i° , a sampled position s_j on r_i° , and a 3D neighbor with position p_j and ray r_j , the list of geometric metadata includes:

- the depth of the crossing $p_1(r_i^\circ, r_j)$ with respect to the current camera
- the depth of the sampled position s_j
- the depth difference between p_1 and the sampled position s_j
- the distance between s_j and r_j : $\min_{p \in \mathcal{R}_j} \|p - s_j\|$
- the distance between the two rays: $\|p_1 - p_2\|$
- the distance between p_1 and p_j : $\|p_j - p_1\|$
- the distance between s_j and p_j : $\|p_j - s_j\|$
- the distance between p_1 and the current camera
- the distance between p_2 and the originating camera of p_j : $\|p_2 - (p_j - z_j \cdot r_j)\|$
- the cosine ray angle between r_i° and r_j : $r_i^\circ \cdot r_j$
- the cosine ray angle between r_i° and the ray connecting s_j and the originating camera of p_j : $r_i^\circ \cdot \frac{(s_j - (p_j - z_j \cdot r_j))}{\|(s_j - (p_j - z_j \cdot r_j))\|}$
- the probability density at p_2 within the Gaussian distribution centered at p_j with standard deviation σ_j : $\frac{1}{\sigma_j \sqrt{2\pi}} \exp(-\frac{1}{2}(\frac{p_2 - p_j}{\sigma_j})^2)$

- a binary mask indicating whether p_j lies in front of the current camera

Similar to the scene update step, we concatenate the metadata with the reduced 3D features and the feature dot products at each sampled position, passing them through a small MLP. The outputs from all sampled positions are then combined with the reduced feature of p_i° , and this combined vector is processed by another small MLP to produce h_i , which represents the information p_i° has gained from the scene point cloud.

Finally, we apply a small U-Net to aggregate features across all levels, similar to the scene update step. From the updated features h_i , we directly predict the depth values d_i , the standard deviation σ_i and the confidence score c_i using a linear layer. At levels other than the coarsest, we utilize the depth predictions from the coarser levels for guidance. Each point at these levels gathers predicted depths from nearby points in the coarser feature map, interpolates them using inverse distance weighting, and appends the result to h_i before making the final depth prediction. Additionally, We append h_i to the original 2D point features f_i , feeding them through a linear layer to generate the final updated features. The 2D points are then back-projected into 3D space using the predicted depth, and this new set of points is added to the existing scene point cloud.

3.4. Point Cloud Merging

While the overlap in the source images is necessary for stereo matching, it also causes redundancy in the point cloud. When a 2D point successfully matches with a 3D point, both represent the same surface area, while ideally, we would like to keep only one of them. This leads to our point cloud merging step.

First, we find all the cameras in the history whose camera frustum has overlap with the current camera frustum. Then, we project the points in the current camera frustum onto the image planes of these cameras. During training, to train c_i , we first render the depth value at each pixel p_i° by interpolating the depth of the points with the c_i :

$$d_i = \sum_{P(\mathbf{q}_j, \mathbf{I}_t) = p_i^\circ} \text{softmax}(c_j) d_j \quad (3)$$

where $P(\mathbf{q}_j, \mathbf{I}_t)$ projects \mathbf{q}_j to the image plane of \mathbf{I}_t . Thus, for the model to render the correct depth, it needs to boost the c_i of a point on the true surface and reduce c_i of those points at incorrect location. Then, we trim the point cloud by only keeping the point with the highest confidence score at each pixel. During inference, we keep the point with minimal depth to the camera at each pixel p_i° :

$$d_i = \min_{\substack{P(\mathbf{q}_j, \mathbf{I}_t) = p_i^\circ \\ c_j > \epsilon}} d_j \quad (4)$$

where ϵ is empirically set to 0. The value d_i is also used as

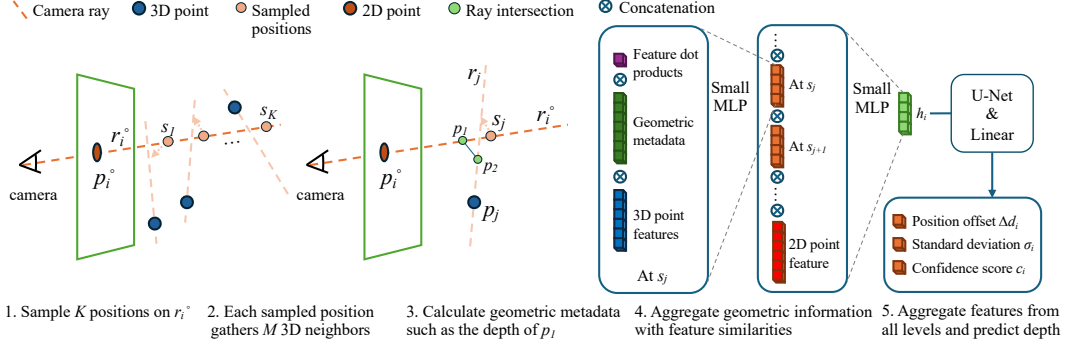


Figure 3. **Illustration of the depth prediction step** (single level shown for simplicity). For a 2D feature point p_i^o on the image plane, we uniformly sample K positions along its camera ray. Each sampled position identifies M neighboring points in the point cloud by finding the nearest rays. For each neighbor, we compute its feature dot product with p_i^o , along with geometric metadata such as the depth at the crossing of the rays. The 2D point uses both geometric data and feature similarities to predict its depth value.

the rendered depth value from the point cloud during evaluation.

Note that while we train the model using 9-view local windows, our goal is to seamlessly reconstruct the entire scene during evaluation. As the sequence length increases, the number of cameras sharing a partial view can reach into the hundreds, leading to a significant computational burden. To address this, we employ a heuristic: if a camera is not among the K most recent cameras in the current merging step, we retain all points covering the pixels of that camera, preventing their deletion, and remove the camera from the current merging algorithm. We empirically set $K = 16$.

3.5. Loss Functions

We train our model by supervising the depth maps produced by different modules of our model: the monocular depth prediction, the depth prediction with feature matching and the depth maps rendered at the point merging step. The three types of depth maps use the same set of losses: an $L1$ depth loss, a gradient loss and a normal loss following [26].

We apply the $L1$ depth loss

$$\mathcal{L}_{\text{depth}} = \frac{1}{HW} \sum_{l=1}^4 \frac{1}{l^2} \sum_i |\log d_i^l - \log d_i^{\text{gt}}| \quad (5)$$

to all four levels. We upsample the depth values from the coarse levels to full resolution using inverse distance weighted interpolation. We apply the gradient loss

$$\mathcal{L}_{\text{grad}} = \frac{1}{HW} \sum_{r=0}^3 \sum_i |\nabla d_{i \downarrow 2^r \times}^4 - \nabla d_{i \downarrow 2^r \times}^{\text{gt}}| \quad (6)$$

to only the finest level, but both to the full resolution and to the three downsampled versions (we downsample the resolution by half each time). ∇ represents the first-order spatial gradients, and $\downarrow_{2^r \times}$ means downsampling by a rate of 2^r . We also apply the normal loss

$$\mathcal{L}_{\text{normal}} = \frac{1}{2HW} \sum_i 1 - \mathbf{N}_i \cdot \mathbf{N}_i^{\text{gt}} \quad (7)$$

to the finest level, where \mathbf{N}_i is the normal vector calculated from predicted depth and camera intrinsics. Additionally, to supervise the scene update step, we calculate the difference between the distance from each point to its camera and the ground-truth value:

$$\mathcal{L}_{\text{update}} = \frac{1}{N} \sum_{l=1}^4 |z_i - z_i^{\text{gt}}| \quad (8)$$

where z_i is the distance to the camera computed from the predicted 3D position p_i and z_i^{gt} is the ground truth distance. N is the total number of points from all 4 levels. Overall, our total loss is

$$\mathcal{L}_{\text{total}} = \mathcal{L}_{\text{depth}} + \mathcal{L}_{\text{grad}} + \mathcal{L}_{\text{normal}} + \mathcal{L}_{\text{update}} \quad (9)$$

4. Experiments

4.1. Implementation Details

We select AFF-Mini, the smallest variant from [40] consisting of only 6.75M parameters, as our image encoder backbone. Our model is trained and evaluated on the ScanNetv2 [7] dataset. We resize the input resolution to 640×480 . The finest-level depth maps are predicted at a resolution of 160×120 , creating 19,200 points each new frame.

Model hyperparameters. In both the scene update step and the depth prediction step, we set the sample number $K = 32$ and number of neighbors $M = 1$. The sampling range is configured to be 1.5m, while the point update offset range is limited to 5m. Following the design of AFF, all transformer blocks in the model perform local attention with a neighborhood size of 48 and an MLP expansion ratio of 2.0 by default. When level i attends to a coarser level j , the neighborhood size is reduced to $\max(4, \frac{48}{4^{i-j}})$.

Relative position embedding. Within the 2D local attention layers, we follow AFF by embedding the relative position between two points p_i^o and p_j^o using the position

Recon Type	Method	Non-Volumetric	Latency (ms/frame)	Abs Diff↓	Abs Rel↓	Sq Rel↓	$\delta < 1.05\uparrow$	$\delta < 1.25\uparrow$	Comp↑
Offline	COLMAP [27]	✓	/	0.264	0.137	0.138	-	83.4	87.1
	Atlas [23]	✗	/	0.123	0.065	0.045	-	93.6	99.9
	VoRTX [28]	✗	/	0.092	0.058	0.036	-	93.8	95.0
	CVRecon [9]	✗	/	0.078	0.047	0.028	-	96.3	-
	FineRecon [29]	✗	/	0.069	0.042	0.026	86.6	97.1	97.2
Online	NeuralRecon [30]	✗	90	0.106	0.065	0.031	-	94.8	90.9
	TF [1]	✗	326	0.099	0.065	0.042	-	93.4	90.5
	SimpleRecon [26]	✓	72	0.083	0.046	0.022	-	95.4	94.4
	PointRecon (4cm)	✓	618	0.085	0.054	0.022	71.9	96.4	94.8
	PointRecon (2cm)	✓	618	0.087	0.055	0.024	72.1	96.2	94.6

Table 1. **Depth Map Evaluation.** Depth map quality for the ScanNetv2 test split, rendered from the reconstructed 3D meshes. We follow the evaluation protocol of Atlas [23]. - indicates that the metric was not reported in the original paper. Offline methods assume access to the entire sequence and do not support local updates. The numbers in brackets indicate the TSDF Fusion resolution. While we present results for both 2cm and 4cm resolutions (with 4cm commonly used in volumetric methods), our point-based representation is not constrained by any specific TSDF Fusion resolution.

Recon Type	Method	Comp↓	Acc↓	Chamfer↓	Prec↑	Recall↑	F-Score↑
Offline	COLMAP	0.069	0.135	0.102	0.634	0.505	0.558
	Atlas	0.084	0.102	0.093	0.598	0.565	0.578
	VoRTX	0.082	0.062	0.072	0.688	0.607	0.644
	CVRecon	0.077	0.045	0.061	0.753	0.639	0.690
Online	DeepVMVS	0.076	0.117	0.097	0.451	0.558	0.496
	NeuralRecon	0.128	0.054	0.091	0.684	0.479	0.562
	TF	0.099	0.078	0.089	0.648	0.547	0.591
	SimpleRecon	0.078	0.065	0.072	0.641	0.581	0.608
	VisFusion	0.105	0.055	0.080	0.695	0.527	0.598
	PointRecon (4cm)	0.082	0.086	0.084	0.568	0.556	0.560
	PointRecon (2cm)	0.073	0.083	0.078	0.586	0.612	0.599

Table 2. **Mesh Evaluation.** Mesh reconstruction quality for the ScanNetv2 test split, following the evaluation protocol of Atlas [23]. The number in parentheses represents the TSDF Fusion resolution.

difference $p_i^\circ - p_j^\circ$, the distance $\|p_i^\circ - p_j^\circ\|$, and the sine and cosine of the angle between $p_i^\circ - p_j^\circ$ and the positive x -axis. In the 3D local attention layers, for two points p_i and p_j , we similarly embed their relative position, but replace the 2D angular components with the sine and cosine values of the angle between $p_i - p_j$ and the ground plane.

Training details. We begin with training the model on image pairs for 2 epochs, using the two images to mutually serve as sources for feature matching, without any point merging at this stage. Then, we train the model on 9-view local image windows for 6 epochs, feeding the images sequentially into the model and performing point merging at each time step. We use a learning rate 10^{-4} for the first 4 epochs, reducing it by a factor of 0.1 at the fifth epoch and the eighth epoch. We train with the AdamW optimizer [19] with a weight decay of 10^{-4} .

During training, we apply random color augmentation to the input RGB images with a probability of 0.8, using TorchVision [21]. The color augmentation parameters include brightness set to 0.4, contrast to 0.4, saturation to 0.2,

and hue to 0.1. Additionally, we randomly reverse the order of the input sequences with a probability of 0.5. For keyframe selection, we follow the methodology outlined in [8]. We reduce the weight for the loss of monocular depth prediction by a factor of 0.5 at the fifth and eighth epochs.

Evaluation details. During evaluation, we sequentially feed the keyframe images into the model, performing point merging at each time step. Once the point cloud for the entire scene is constructed, we render depth maps using the keyframe cameras by projecting the points onto the image planes. Each pixel in the rendered depth maps corresponds to the depth of the closest point (as detailed in Sec. 3.4). To construct a 3D mesh from the rendered depth maps, we apply TSDF fusion [6].

4.2. Experiment Results

ScanNet. ScanNetv2 [7] is an indoor RGB-D video dataset comprising scans of 1,613 rooms, with 1,201 rooms designated for training, 312 for validation, and 100 for testing. Each scan typically includes thousands of image frames, with approximately 1/10 of the frames designated as keyframes. We compare our results with previous work in terms of both 2D depth map quality (Table 1) and 3D mesh quality (Table 2), where the depth maps are rendered from the reconstructed 3D meshes. To showcase the flexibility of our point representation, we generate meshes at two TSDF fusion resolutions, 2cm and 4cm, demonstrating that our approach is not constrained by TSDF resolution. As shown in the tables, our model achieves competitive performance among online methods, particularly excelling in depth map metrics such as “Abs Diff” and “ $\delta < 1.25$,” and delivering comparable results in Chamfer distance and F-score. Additionally, our method uniquely offers resolution flexibility and viewpoint consistency, attributes not captured by standard evaluation metrics. A notable strength of our approach is its top-ranking recall score among all online methods, highlighting our model’s ability to achieve high

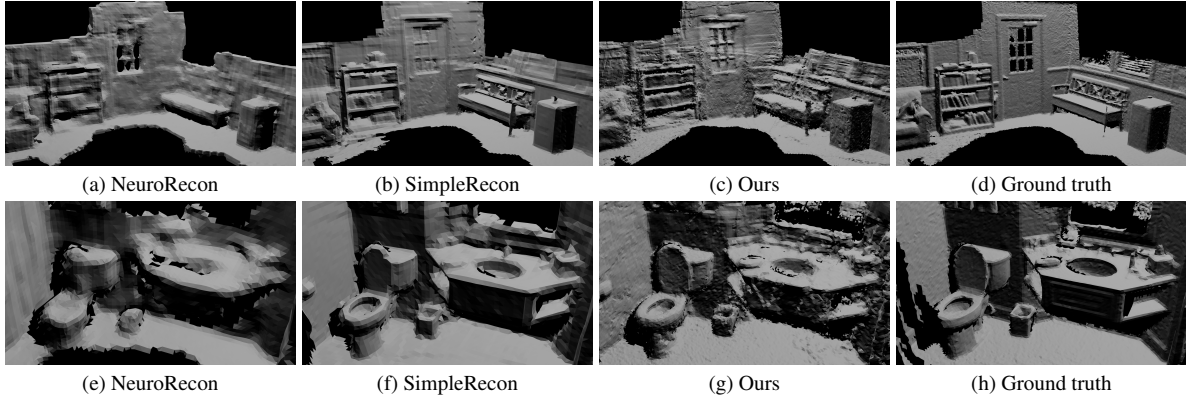


Figure 4. Visualization of generated meshes (please magnify when viewing). We first render depth maps from the scene point cloud and then fuse them using TSDF fusion to generate mesh. Our method produces more detailed reconstructions compared to previous work, though less smooth surfaces may result from the inherent discrete nature of point clouds. **Check out our project page <https://arthurhero.github.io/projects/pointrecon/> for incremental reconstruction videos.**

coverage of ground-truth surfaces. However, a lower precision score reflects some surface redundancy in the reconstructed meshes. This issue stems from the current merging heuristic, which retains points from earlier camera views. While this strategy ensures robust coverage, it may also preserve outdated or less accurate points, leading to redundant surfaces. Addressing this limitation is a promising direction for future optimization.

Profiling. Following [26], we measure the inference speed of our model on a single A100 GPU. On average, the image encoder incurs a latency of 1.8ms per image. The monocular depth predictor requires 8ms, the scene update step takes 215ms, depth prediction with feature matching takes 276ms, and the point merging step adds 118ms. The most computationally intensive component is the transformer U-Net, used in both the scene update and depth prediction steps. The merging process also becomes slower as the point cloud grows. While point-based representations eliminate grid constraints, they introduce computational challenges, particularly in K nearest neighbor searches, which become slower as the point cloud scales. To enhance efficiency, future work will prioritize simplifying the network architecture and further reducing the point cloud size. It is important to note that, despite these computational demands, our approach remains an online method capable of continuously updating the scene with new inputs. In contrast, offline methods require access to the entire sequence before reconstruction, learning features from all images jointly, which inherently imposes an upper limit on sequence length.

Ablation. We analyze the contributions of different components of our model by evaluating the quality of the depth maps produced by these components on the ScanNet test split key frames. To assess the necessity of the scene update step, we train an additional model without this component. As shown in Table 3, feature matching significantly

Scene Update	Model Component	Abs Diff↓	Abs Rel↓	Sq Rel↓	$\delta < 1.05\uparrow$	$\delta < 1.25\uparrow$
Off	Monocular	0.206	0.134	0.053	29.7	82.8
	Feature Matching	0.130	0.083	0.028	50.7	93.3
	Merging	0.109	0.096	0.023	57.8	95.5
On	Monocular	0.206	0.134	0.053	29.7	82.8
	Feature Matching	0.113	0.071	0.024	58.4	94.5
	Merging	0.085	0.053	0.017	69.9	97.0

Table 3. **Ablation studies.** Depth map quality on the ScanNet test split key frames produced by different components of our model. The results show that both the Feature Matching and the Merging modules consistently enhance depth prediction quality. The importance of the Scene Update step is demonstrated by the consistent decrease in the depth map quality when it is omitted (Scene Update does not affect the monocular depth prediction as expected).

improves depth prediction accuracy compared to monocular prediction. Point merging further enhances the accuracy by leveraging predictions from multiple cameras, mitigating ambiguities that a single camera might face. The confidence-based merging results in a higher-quality point cloud. The scene update step is also crucial, as it refines the point cloud, leading to more accurate feature matching and merging in subsequent steps.

5. Conclusion

We propose PointRecon, an online, point-based 3D reconstruction method that incrementally updates a global point cloud from posed monocular RGB images. Our approach offers flexible local updates without the need for predefined resolutions or scene sizes, while ensuring surface consistency across views. A key contribution is the ray-based 2D-3D matching strategy, which improves feature matching robustness. Future work will focus on simplifying the architecture, reducing point cloud size, and refining the merging algorithm to enhance efficiency and performance.

References

- [1] Aljaz Bozic, Pablo Palafox, Justus Thies, Angela Dai, and Matthias Nießner. Transformerfusion: Monocular rgb scene reconstruction using transformers. *Advances in Neural Information Processing Systems*, 34:1403–1414, 2021. 1, 2, 7
- [2] Jia-Ren Chang and Yong-Sheng Chen. Pyramid stereo matching network. In *Proceedings of the IEEE conference on computer vision and pattern recognition*, pages 5410–5418, 2018. 1, 2
- [3] David Charatan, Sizhe Lester Li, Andrea Tagliasacchi, and Vincent Sitzmann. pixelsplat: 3d gaussian splats from image pairs for scalable generalizable 3d reconstruction. In *Proceedings of the IEEE/CVF Conference on Computer Vision and Pattern Recognition*, pages 19457–19467, 2024. 3
- [4] Rui Chen, Songfang Han, Jing Xu, and Hao Su. Point-based multi-view stereo network. In *Proceedings of the IEEE/CVF international conference on computer vision*, pages 1538–1547, 2019. 1, 3
- [5] Yuedong Chen, Haoqi Xu, Chuanxia Zheng, Bohan Zhuang, Marc Pollefeys, Andreas Geiger, Tat-Jen Cham, and Jianfei Cai. Mvsplat: Efficient 3d gaussian splatting from sparse multi-view images. *arXiv preprint arXiv:2403.14627*, 2024. 3
- [6] Brian Curless and Marc Levoy. A volumetric method for building complex models from range images. In *Proceedings of the 23rd annual conference on Computer graphics and interactive techniques*, pages 303–312, 1996. 7
- [7] Angela Dai, Angel X Chang, Manolis Savva, Maciej Halber, Thomas Funkhouser, and Matthias Nießner. Scannet: Richly-annotated 3d reconstructions of indoor scenes. In *Proceedings of the IEEE conference on computer vision and pattern recognition*, pages 5828–5839, 2017. 6, 7
- [8] Arda Duzceker, Silvano Galliani, Christoph Vogel, Pablo Speciale, Mihai Dusmanu, and Marc Pollefeys. Deepvideomvs: Multi-view stereo on video with recurrent spatio-temporal fusion. In *Proceedings of the IEEE/CVF Conference on Computer Vision and Pattern Recognition*, pages 15324–15333, 2021. 1, 2, 7
- [9] Ziyue Feng, Liang Yang, Pengsheng Guo, and Bing Li. Cvrecon: Rethinking 3d geometric feature learning for neural reconstruction. In *Proceedings of the IEEE/CVF International Conference on Computer Vision*, pages 17750–17760, 2023. 3, 7
- [10] Huiyu Gao, Wei Mao, and Miaomiao Liu. Visfusion: Visibility-aware online 3d scene reconstruction from videos. In *Proceedings of the IEEE/CVF Conference on Computer Vision and Pattern Recognition*, pages 17317–17326, 2023. 1, 2
- [11] Kaiming He, Xiangyu Zhang, Shaoqing Ren, and Jian Sun. Deep residual learning for image recognition. In *Proceedings of the IEEE conference on computer vision and pattern recognition*, pages 770–778, 2016. 3
- [12] Po-Han Huang, Kevin Matzen, Johannes Kopf, Narendra Ahuja, and Jia-Bin Huang. Deepmvs: Learning multi-view stereopsis. In *Proceedings of the IEEE conference on computer vision and pattern recognition*, pages 2821–2830, 2018. 1, 2
- [13] Sunghoon Im, Hae-Gon Jeon, Stephen Lin, and In So Kweon. Dpsnet: End-to-end deep plane sweep stereo. *arXiv preprint arXiv:1905.00538*, 2019. 1, 2
- [14] Jihong Ju, Ching Wei Tseng, Oleksandr Bailo, Georgi Dikov, and Mohsen Ghafoorian. Dg-recon: Depth-guided neural 3d scene reconstruction. In *Proceedings of the IEEE/CVF International Conference on Computer Vision*, pages 18184–18194, 2023. 3
- [15] Abhishek Kar, Christian Häne, and Jitendra Malik. Learning a multi-view stereo machine. *Advances in neural information processing systems*, 30, 2017. 1, 2
- [16] Alex Kendall, Hayk Martirosyan, Saumitro Dasgupta, Peter Henry, Ryan Kennedy, Abraham Bachrach, and Adam Bry. End-to-end learning of geometry and context for deep stereo regression. In *Proceedings of the IEEE international conference on computer vision*, pages 66–75, 2017. 1, 2
- [17] Bernhard Kerbl, Georgios Kopanas, Thomas Leimkühler, and George Drettakis. 3d gaussian splatting for real-time radiance field rendering. *ACM Transactions on Graphics*, 42(4):1–14, 2023. 1, 3
- [18] Maxime Lhuillier and Long Quan. A quasi-dense approach to surface reconstruction from uncalibrated images. *IEEE transactions on pattern analysis and machine intelligence*, 27(3):418–433, 2005. 1, 3
- [19] Ilya Loshchilov and Frank Hutter. Decoupled weight decay regularization. *arXiv preprint arXiv:1711.05101*, 2017. 7
- [20] Wenjie Luo, Alexander G Schwing, and Raquel Urtasun. Efficient deep learning for stereo matching. In *Proceedings of the IEEE conference on computer vision and pattern recognition*, pages 5695–5703, 2016. 2
- [21] Sébastien Marcel and Yann Rodriguez. Torchvision the machine-vision package of torch. In *Proceedings of the 18th ACM international conference on Multimedia*, pages 1485–1488, 2010. 7
- [22] Raul Mur-Artal, Jose Maria Martinez Montiel, and Juan D Tardos. Orb-slam: a versatile and accurate monocular slam system. *IEEE transactions on robotics*, 31(5):1147–1163, 2015. 2
- [23] Zak Murez, Tarrence Van As, James Bartolozzi, Ayan Sinha, Vijay Badrinarayanan, and Andrew Rabinovich. Atlas: End-to-end 3d scene reconstruction from posed images. In *Computer Vision–ECCV 2020: 16th European Conference, Glasgow, UK, August 23–28, 2020, Proceedings, Part VII 16*, pages 414–431. Springer, 2020. 1, 2, 7
- [24] Richard A Newcombe, Steven J Lovegrove, and Andrew J Davison. Dtam: Dense tracking and mapping in real-time. In *2011 international conference on computer vision*, pages 2320–2327. IEEE, 2011. 2
- [25] Matia Pizzoli, Christian Forster, and Davide Scaramuzza. Remode: Probabilistic, monocular dense reconstruction in real time. In *2014 IEEE international conference on robotics and automation (ICRA)*, pages 2609–2616. IEEE, 2014. 2
- [26] Mohamed Sayed, John Gibson, Jamie Watson, Victor Prisacariu, Michael Firman, and Clément Godard. Simplerecon: 3d reconstruction without 3d convolutions. In *European*

- Conference on Computer Vision*, pages 1–19. Springer, 2022. [1](#), [2](#), [6](#), [7](#), [8](#)
- [27] Johannes L Schönberger, Enliang Zheng, Jan-Michael Frahm, and Marc Pollefeys. Pixelwise view selection for unstructured multi-view stereo. In *Computer Vision–ECCV 2016: 14th European Conference, Amsterdam, The Netherlands, October 11–14, 2016, Proceedings, Part III 14*, pages 501–518. Springer, 2016. [7](#)
- [28] Noah Stier, Alexander Rich, Pradeep Sen, and Tobias Höllerer. Vortex: Volumetric 3d reconstruction with transformers for voxelwise view selection and fusion. In *2021 International Conference on 3D Vision (3DV)*, pages 320–330. IEEE, 2021. [1](#), [3](#), [7](#)
- [29] Noah Stier, Anurag Ranjan, Alex Colburn, Yajie Yan, Liang Yang, Fangchang Ma, and Baptiste Angles. Finerecon: Depth-aware feed-forward network for detailed 3d reconstruction. *arXiv preprint arXiv:2304.01480*, 2023. [3](#), [7](#)
- [30] Jiaming Sun, Yiming Xie, Linghao Chen, Xiaowei Zhou, and Hujun Bao. Neuralrecon: Real-time coherent 3d reconstruction from monocular video. In *Proceedings of the IEEE/CVF Conference on Computer Vision and Pattern Recognition*, pages 15598–15607, 2021. [1](#), [2](#), [7](#)
- [31] Jiayang Tang, Zhaoxi Chen, Xiaokang Chen, Tengfei Wang, Gang Zeng, and Ziwei Liu. Lgm: Large multi-view gaussian model for high-resolution 3d content creation. *arXiv preprint arXiv:2402.05054*, 2024. [3](#)
- [32] Zachary Teed and Jia Deng. Droid-slam: Deep visual slam for monocular, stereo, and rgb-d cameras. *Advances in neural information processing systems*, 34:16558–16569, 2021. [2](#)
- [33] Kaixuan Wang and Shaojie Shen. Mvdepthnet: Real-time multiview depth estimation neural network. In *2018 International conference on 3d vision (3DV)*, pages 248–257. IEEE, 2018. [1](#), [2](#)
- [34] Yao Yao, Zixin Luo, Shiwei Li, Tian Fang, and Long Quan. Mvsnet: Depth inference for unstructured multi-view stereo. In *Proceedings of the European conference on computer vision (ECCV)*, pages 767–783, 2018. [1](#), [2](#)
- [35] Jure Zbontar and Yann LeCun. Stereo matching by training a convolutional neural network to compare image patches. *Journal of Machine Learning Research*, 17, 2016. [2](#)
- [36] Kai Zhang, Sai Bi, Hao Tan, Yuanbo Xiangli, Nanxuan Zhao, Kalyan Sunkavalli, and Zexiang Xu. Gs-lrm: Large reconstruction model for 3d gaussian splatting. *arXiv preprint arXiv:2404.19702*, 2024. [3](#)
- [37] Youmin Zhang, Fabio Tosi, Stefano Mattoccia, and Matteo Poggi. Go-slam: Global optimization for consistent 3d instant reconstruction. In *Proceedings of the IEEE/CVF International Conference on Computer Vision*, pages 3727–3737, 2023. [2](#)
- [38] Heng Zhou, Zhetao Guo, Shuhong Liu, Lechen Zhang, Qihao Wang, Yuxiang Ren, and Mingrui Li. Mod-slam: Monocular dense mapping for unbounded 3d scene reconstruction. *arXiv preprint arXiv:2402.03762*, 2024.
- [39] Zihan Zhu, Songyou Peng, Viktor Larsson, Zhaopeng Cui, Martin R Oswald, Andreas Geiger, and Marc Pollefeys. Nicer-slam: Neural implicit scene encoding for rgb slam. In *2024 International Conference on 3D Vision (3DV)*, pages 42–52. IEEE, 2024. [2](#)
- [40] Chen Ziwen, Kaushik Patnaik, Shuangfei Zhai, Alvin Wan, Zhile Ren, Alexander G Schwing, Alex Colburn, and Li Fuxin. Autofocusformer: Image segmentation off the grid. In *Proceedings of the IEEE/CVF Conference on Computer Vision and Pattern Recognition*, pages 18227–18236, 2023. [3](#), [6](#)
- [41] Chen Ziwen, Hao Tan, Kai Zhang, Sai Bi, Fujun Luan, Yicong Hong, Li Fuxin, and Zexiang Xu. Long-lrm: Long-sequence large reconstruction model for wide-coverage gaussian splats. *arXiv preprint 2410.12781*, 2024. [3](#)